



RESEARCH ARTICLE

System identification of a hovering quadrotor biplane tailsitter with canted motors

O. Juhasz¹, J-P. Reddinger² and J. Whitt^{3,†}

¹Aerospace Engineering Department, United States Naval Academy, Annapolis, MD, USA

²DEVCOM Army Research Laboratory, Aberdeen Proving Ground, Aberdeen, MD, USA

³Department of Mechanical and Aerospace Engineering, North Carolina State University, Raleigh, NC, USA

Corresponding author: J. Whitt; Email: juhasz@usna.edu

Received: 3 October 2024; **Revised:** 19 February 2025; **Accepted:** 26 March 2025

Keywords: flight dynamics; system identification; UAS; e-VTOL

Abstract

A quadrotor was modified by adding wings to the frame to directly compare the flight dynamics characteristics as well as the stability and control derivatives of the quadrotor and its biplane tailsitter variant. The on-axis response of the quadrotor and a biplane tailsitter variant were measured through flight tests, and a frequency domain system identification was used for non-parametric and parametric model identification. Identification of the full vehicle dynamics also demonstrated that identifying the motor torque and back-EMF constants from no-load measurements and the remaining motor parameters from a rotor-motor test stand provided the most accurately identified full vehicle model. The motor dynamics were shown to add a pole to the thrust-based responses (roll, pitch and heave), while the torque-based response (yaw) included a pole and a zero. This approach was then used to identify and compare the quadrotor dynamics, tailsitter dynamics and the total impact of canting the motors. It was found that the presence of the wing added pitch damping to the dynamics and pitch stability became negative. The yaw axis saw an increase in yaw damping derivative, and a reduction in the yaw control derivative to the point where it became difficult to control the aircraft. By introducing cant, both the quadrotor and tailsitter saw large increases in the yaw control derivative. Further, the rotor thrust-based moment generation due to cant resulted in the yaw response zero being canceled by the motor dynamics, resulting in a purely first-order yaw response. Neither the wing nor cant produced any change in the lateral and heave axes.

Nomenclature

a_z	vehicle vertical acceleration (m/s)
B	motor drag coefficient (N-m-s)
i	motor input current (A)
I	moment of inertia (kg-m ²)
K_e	motor back-EMF constant (V-s/rad)
K_T	motor torque constant (N-m/A)
K_V	motor speed constant (RPM/V)
L_a	equivalent motor armature inductance (H)
L_p	roll damping derivative
L_v	roll stability derivative
$L_{\delta_{int}}$	roll moment control derivative

[†] SMART Scholar at DEVCOM Army Research Laboratory

M_u	pitch stability derivative
M_q	pitch damping derivative
$M_{\delta_{lon}}$	pitch moment control derivative
N_r	yaw damping derivative
$N'_{\delta_{dir}}$	yaw control derivative before motor
$N_{\delta_{dir}}$	yaw control derivative after motor
p	vehicle roll rate (rad/s)
q	vehicle pitch rate (rad/s)
Q_A	aerodynamic torque (N-m)
Q_T	total rotor torque (N-m)
r	vehicle yaw rate (rad/s)
R_a	equivalent motor armature resistance (Ω)
T	total rotor thrust (N)
V	motor input voltage (V)
x	longitudinal body axis, positive forward (m)
X_u	longitudinal damping derivative
y	lateral body axis, positive right (m)
Y_v	lateral damping derivative
z	vertical body axis, positive down (m)
Z_w	heave damping derivative
$Z_{\delta_{col}}$	heave control derivative
δ_{lat}	lateral control input
δ_{lon}	longitudinal control input
δ_{dir}	directional control input
δ_{col}	collective control input
γ	boom cant angle rotation about the torsional axis
τ	motor state
ω_{mot}	motor mechanical system pole
ω_{elec}	motor electrical system pole
ω_{lead}	motor torque response zero
Ω	rotor speed (rad/s)

1.0 Introduction

Advances in battery and electric motor technology have enabled the design space of unmanned aerial systems (UAS) with gross weights of up to 1,000 lb. Within this new design space, novel configurations are being explored that were previously infeasible or suboptimal for crewed aircraft, such as tailsitter aircraft. Tailsitter configurations have existed since the mid-20th century, with early examples including the Convair XFY-1 and the Lockheed XFV-1. These designs are typically driven by the desire for a vertical take-off and landing (VTOL) capability paired with the forward flight speeds and cruise efficiency of a fixed-wing aircraft. While originally developed as full-scale vehicles, the requirement for pilots to operate the vehicle facing the air during descent and landing contributed to a decline in interest in this configuration in favour of tilt rotor aircraft.

Modern permutations of the tail sitter design focus on UAS-relevant scales where the use of remote or autonomous piloting eliminates many of the issues associated with rigid body rotation through the flight. The reduced scale has opened up the design space and led to the introduction of electric drive trains, new control strategies and configurations that were not feasible at larger scales. Research vehicles in the 1–5 lb. range include the UMD Quadrotor Biplane Tailsitter (QBiT) [1, 2], the DEVCOM ARL Common Research Configuration (CRC) [3, 4], and incorporate fixed pitch rotors at variable RPM for vehicle control, while the 20 lb. variant of the CRC optionally uses collective pitch control on each rotor. The Bell Autonomous Pod Transport (APT-70) has a gross weight of over 360 lb and incorporates control surfaces in the wake of the rotors for additional moment authority. Current and past Defense Advanced Research Projects Agency (DARPA) projects have also begun to investigate the design space



Figure 1. Quadrotor showing Hexsoon EDU-450 frame and custom foam wings.

of such vehicles, including Tactically Exploited Reconnaissance Node (TERN) at roughly 600 lb, and the ongoing AdvanCed airCRAFT Infrastructure-Less Launch And RecoverY (ANCILLARY).

Over the entire range of scales that are now being explored, there are steady and dynamic implications of transitioning a large wing through a large range of pitching motion in the wake of multiple rotors, which are still not well understood. Some initial work has been done to attempt to analyse the steady component of interactional aerodynamics of the rotors on the wings [5], as well as simulated vehicle trajectories against flight tests with and without unsteady lift generation on the wing [6].

From a control power perspective, it has been qualitatively observed that rotor cant is necessary to maintain adequate yaw control authority of a tailsitter UAS in hover, and roll control authority in forward flight [7], but the quantitative impact on dynamics and handling qualities has never been quantified. Analytical methods have been used to identify the handling qualities implication of rotor cant on an eVTOL scale quadrotor configuration [8], and prototype aircraft at that scale, such as the Wisk Aero Cora, have canted rotors that are oriented in such a way that would augment yaw control.

More recently, an initial examination of the total vehicle dynamics of the tailsitter aircraft pictured in Fig. 1 was conducted in the longitudinal and lateral axes. The resulting system identification-based models showed large impacts from the wings on key stability derivatives in the longitudinal axis. It was also observed that yaw control was difficult to maintain, but a yaw axis identification was not attempted [9].

The goal of this paper is to extend this effort to examine the hovering dynamics of a small quadrotor tailsitter biplane aircraft. This includes a quantitative analysis and comparisons of system-identified vehicle dynamics models obtained from flight tests. Specific goals include the quantification of the impacts of rotor cant angles and the additional yaw authority they generate in hovering flight, as well as the general impacts of the presence of wings and their integrated impact on vehicle dynamics.

2.0 Vehicle Description

2.1 Baseline quadrotor configuration

The baseline quadrotor used in this study is a Hexsoon EDU-450, which is a commercially available hobby-scale quadrotor. It has a gross weight of 1.61 kg, four motors with a reported 880 K_v rating and Master Aircrew 10×4.5 rotors. There is a 5° dihedral angle built into the root of each boom. The planform of the hubs is square with a 44.5 cm hub-to-hub diagonal distance.

Table 1. Properties of the tested aircraft. Reference position is the geometric centre of the four hubs

Property	Quadrotor	Tailsitter
z_{cg}^* (cm)	7.3	7.3
z_{wing}^* (cm)	–	7.3
x_{wing}^* (cm)	–	± 19.4
Wingspan (cm)	–	86
Chord (cm)	–	17
Hub diagonal distance (cm)	44.5	44.5
Boom dihedral	5°	5°
Total mass (kg)	1.61	1.77
I_{xx} (kg-m ²)	0.0301	0.0405
I_{yy} kg-m ²	0.0323	0.0388
I_{zz} kg-m ²	0.0329	0.0491

*Positions are relative with respect to geometric center of rotor hubs. Wing locations denote position of quarter chord.

Geometric measurements of the baseline quadrotor were taken and mass properties were identified using a series of swing tests. These parameters are presented in Table 1. The reference location for the positions given is relative to the geometric centre of the four rotor hubs using the north-east-down body-fixed convention relative to the vehicle’s orientation in hover (z is positive down). There was assumed to be a negligible CG shift with the wings mounted, as the vertical location of the quarter chord of the wing was mounted in line with the baseline quadrotor CG. The wing reference positions are reported relative to their quarter chords.

2.2 Quadrotor biplane tailsitter configuration

For the quadrotor biplane tailsitter configuration, the baseline quadrotor vehicle is modified by attaching two wings to the outer edges of the four landing gear [9], as shown in Fig. 1. The wings have a NACA0012 aerofoil and are cut from a polystyrene foam sheet using a hot-wire foam cutter. The wing mount is constructed to counteract the dihedral angle imposed by the booms, such that the chordlines of the wings are parallel and vertically oriented. The thickness of the mount and mounting location imposes a 3.7 cm longitudinal offset between the centre of the rotor hubs and the chordline of the wings, with the wings being further outboard. The additional wings modify the mass properties of the vehicle, which are also reported in Table 1.

2.3 Motor cant

Custom wedge-shaped 3D printed motor mounts were designed to introduce cant rotations about each boom of 5° and 10° . The motor cant angle is implemented such that the rotor thrust adds with the reaction torque of the motor when resolved at the vehicle centre of gravity. Figure 2 shows how this angle introduces a coupling of thrust in the same direction as the reaction torque generated by the rotor.

The front-right and rear-left rotors rotate counter-clockwise, which produces a clockwise reaction torque. If the front-right motor is rotated about the boom to point 5° towards the rear-right of the aircraft, the portion of the thrust in the vehicle x-y plane will add to its reaction torque when resolved at the centre of gravity, and therefore increase the sensitivity of vehicle torque in the yaw axis to a commanded change in directional input. Similarly, the front-left, rear-left and rear-right motors are canted towards the rear-left, front-left and front-right of the aircraft, respectively.

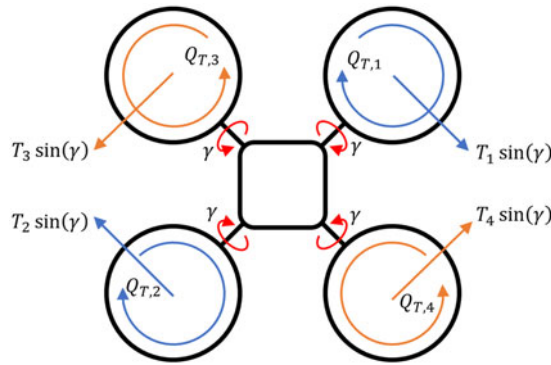


Figure 2. Diagram of cant angles coupling the reaction torque with the yaw axis component of rotor thrust about the CG.

3.0 System Identification Results

The system identification process followed herein was developed by Tischler [10] and packaged into the CIPHER[®] software suite. First, non-parametric models were obtained by running a frequency sweep into a desired input channel. The resulting input and output time histories were windowed and passed through the Fourier transform in the software to generate a frequency response of the input/output pair. Next, state-space models were fit for the parametric identification to a variety of outputs for each input. The resulting responses were assumed to be decoupled, meaning only on axis outputs were used for model fitting. This system identification process has been used successfully in the past on a large variety of UAS [11–13], so additional details are not provided here.

3.1 Motor/rotor subsystem

To better isolate motor dynamics and their impacts on the aircraft response, particularly in the yaw axis, an individual rotor/motor pair was mounted on the test stand shown in Fig. 3 to facilitate system identification of the motor and electrical dynamics. The motor used was a T-Motor Air2216 880 KV motor.

In order to identify high-frequency dynamics, a significantly high sampling rate was necessary. TytoRobotics' commercially available Flight Stand 15 Pro was selected to provide a sampling rate of 1 kHz with a load cell precision in thrust and torque of $\pm 0.5\%$. An optical RPM sensor counts the number of instances the reflective marker passes in front of it, returning RPM with a reported precision of ± 1 RPM. Time signals from the RPM sensor were synced with that of the flight stand and were recorded together.

A frequency sweep of the ESC command, a pulse width modulated (PWM) signal, was performed, with electrical measurements taken of the ESC input voltage and current, as well as rotor thrust, torque and speed. The rotor was first given a 1,500 PWM input signal to represent the nominal trimmed motor operating point. From here, the input frequencies ranged from 0.3 to 35 rad/sec were added to the trimmed signal, maintaining the total PWM value between 1000 and 2000 PWM. The parametric model identification of the coupled motor and rotor dynamics is shown in Fig. 4 [14].

The motor/electrical equations form a pair of coupled differential equations, one governing a first-order representation of the dynamics of the motor electrical circuit (Equation (1)), and the other governing the torque equilibrium of the system (Equation(2)).

$$L_a \dot{i} = -R_a i - K_e \Omega + V \quad (1)$$



Figure 3. Experimental test stand equipment.

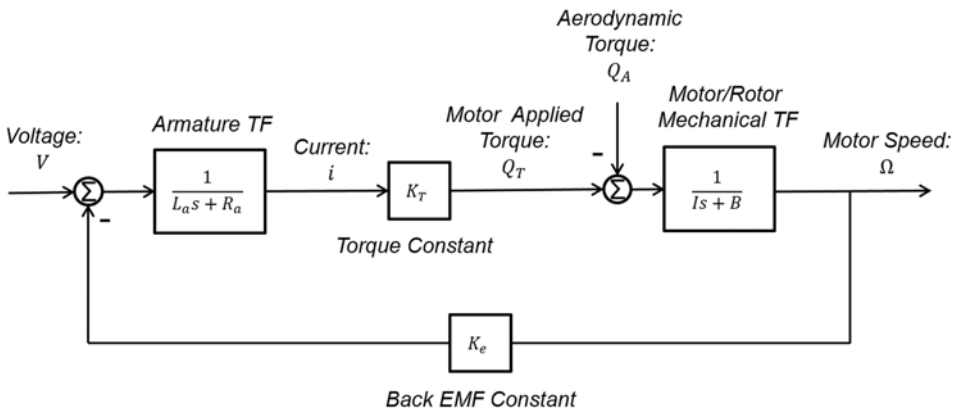


Figure 4. Block diagram of motor/armature dynamics.

$$I\dot{\Omega} = K_T i - Q_A - B\Omega \quad (2)$$

The circuit equation contains the equivalent inductance L_a , equivalent resistance R_a and the back-EMF. The circuit is driven by the applied voltage scaled by the PWM signal and drives the motor through the torque constant, K_T . The torque equation contains the total applied torque by the motor Q_T , the aerodynamic torque from the rotor Q_A , the total inertia of the rotor and motor drives I , and friction B . In the system identification process, the aerodynamic torque Q_A is assumed to vary solely with rotor speed, Ω . Once linearised, this parameter, $\partial Q_A / \partial \Omega$, sums with the internal motor friction. In state-space form, the equations are:

$$\begin{bmatrix} L_a & 0 \\ 0 & I \end{bmatrix} \begin{bmatrix} \dot{i} \\ \dot{\Omega} \end{bmatrix} = \begin{bmatrix} -R_a & -K_e \\ K_T & -(B + \partial Q_A / \partial \Omega) \end{bmatrix} \begin{bmatrix} i \\ \Omega \end{bmatrix} + \begin{bmatrix} 1 \\ 0 \end{bmatrix} [V] \quad (3)$$

Torque and thrust were measured in a load cell below the rotor mount. Therefore, the torque measured is the total torque generated by the motor, not just aerodynamic torque, and includes the inertial and

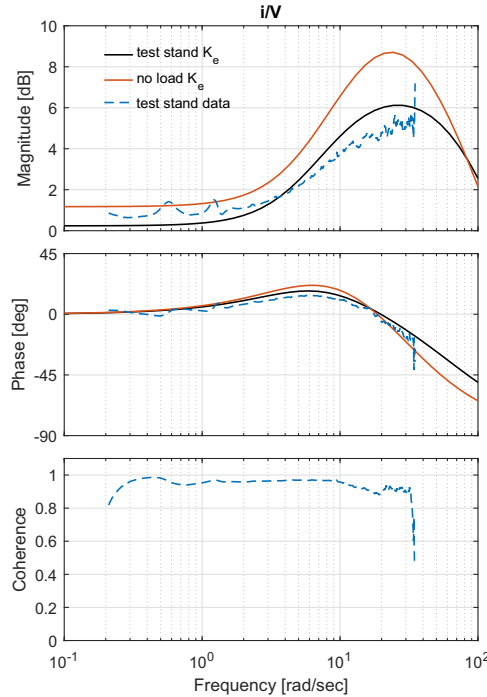


Figure 5. Motor electrical current response to voltage-scaled ESC input. Data taken from a rotor thrust stand.

friction elements as well, $Q_T = K_T i = Q_A + I\dot{\Omega} + B\Omega$. Since the total torque can be obtained from either the current (forcing input) or the rotor speed (forced response), both sets of equations are used in the output equations to improve the parameter identification. The linearised output equations are therefore:

$$\begin{bmatrix} \Omega \\ i \\ Q_T \\ Q_T \\ T \end{bmatrix} = \begin{bmatrix} 0 & 1 \\ 1 & 0 \\ K_T & 0 \\ 0 & B + \partial Q_A / \partial \Omega \\ 0 & \partial T / \partial \Omega \end{bmatrix} \begin{bmatrix} i \\ \Omega \end{bmatrix} + \begin{bmatrix} 0 & 0 \\ 0 & 0 \\ 0 & 0 \\ 0 & I \\ 0 & 0 \end{bmatrix} \begin{bmatrix} \dot{i} \\ \dot{\Omega} \end{bmatrix} \quad (4)$$

CIFER [10] was used to identify the parameters of the equations of motion (Equation (3)). Initially, all the parameters were left free to identify based solely on the test stand sweep data, and the resulting model is compared to test data in Figs. 5–8 with label *test stand* K_e . The first column of parameters in Table 2 shows the identified parameters based on this identification approach. The model resulted in an average mismatch cost between data and model of $J_{ave} = 7.8$, meaning a nearly perfect model was obtained to match the flight test data (average costs of $J_{ave} < 50$ are considered excellent model fits [10]). Often in system identification, time delays are retained to account for computation or processing delays. No such delays were accounted for since all the signals were directly recorded at high sample rates.

A common practice for identifying the motor constants K_e and K_T is to perform a no-load test, measuring RPM as a function of input voltage with no rotor mounted to the motor. In this test, $K_e = \frac{d\Omega}{dV}$ and $K_T = K_e$ for consistent SI units of radians/volt-second, and Newton-meters/ampere. This process yielded a value of $K_T = 0.011$. This is equivalent to a $K_V = \frac{1}{K_T}$ rating of 868, which is close to the reported 880 K_V on the motor casing. A second identification, fixing $K_T = K_e$ to these parameters was also done, and this column is labeled *no load* K_e in Table 2 and subsequent plots. The resulting mismatch cost increased to $J_{avg} = 36$, still giving an overall excellent model. Note that the identified values of K_e and K_T from the

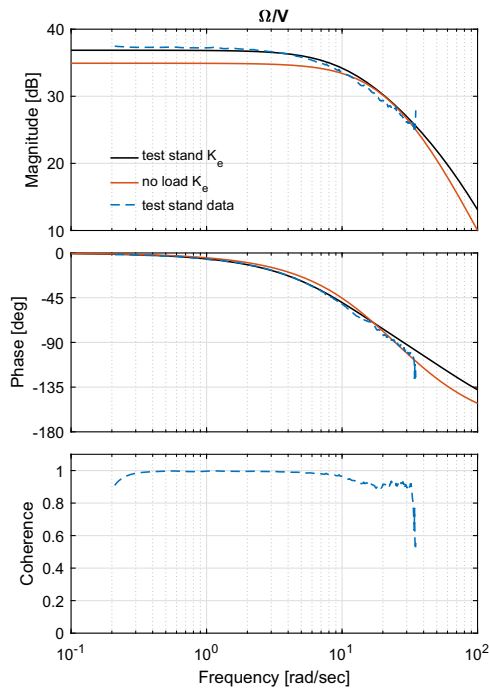


Figure 6. Rotor speed response to voltage-scaled ESC input. Data taken from a rotor thrust stand experiment.

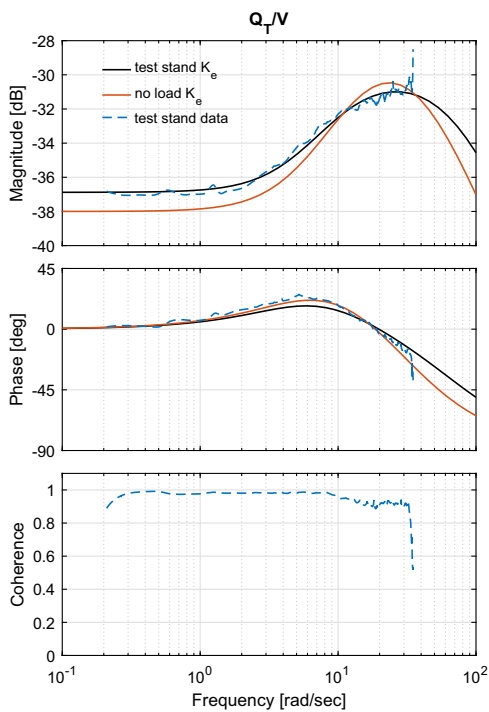


Figure 7. Rotor output torque response to voltage-scaled ESC input. Data taken from a rotor thrust stand experiment.

Table 2. Identified motor constants based on no-load measurement and comprehensive identification

Parameter	test stand K_e	no load K_e	reported value ^b
L_a (H)	6.00×10^{-3}	7.30×10^{-3}	–
K_e (rad/V-s)	7.39×10^{-3}	0.111 ^a	0.011
R_a (Ω)	0.472	0.338	0.115 ± 0.015
I (kg-m ²)	4.14×10^{-5}	4.46×10^{-5}	–
K_T (N-m/A)	0.014	0.011 ^a	0.011
$B + \partial Q_A / \partial \Omega$ (N-m-s)	2.06×10^{-4}	2.26×10^{-4}	N/A

^aHeld constant based on motor subsystem identification.

^bAs reported on t-motor website. $K_T = K_e = 1/K_v$

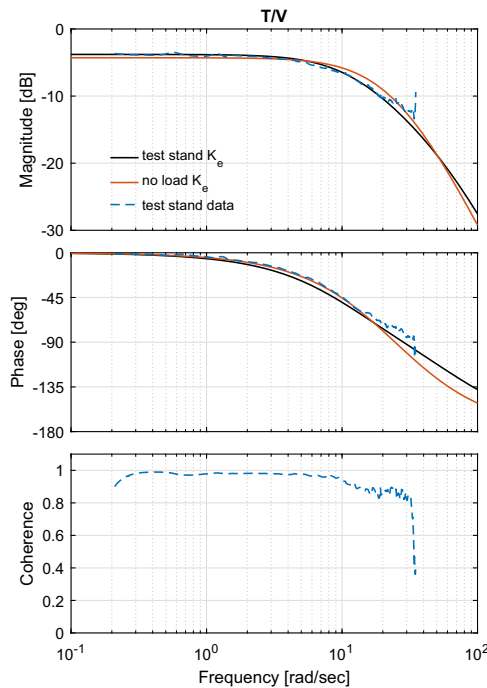


Figure 8. Rotor output thrust response to voltage-scaled ESC input. Data taken from a rotor thrust stand experiment.

initial *test stand* K_e model were 7.39×10^{-3} and 0.014, respectively, which are equivalent to K_v ratings of 1,340 and 680, respectively.

A compressed scale is used on the magnitude plot to highlight the slight differences between the two models in Figs. 5 and 7. Figure 5 shows the motor current to voltage input. The input voltage is scaled by the commanded PWM signal value to be between zero and the supply voltage. The current dynamics include a zero and two poles. Since the current drives the torque through the torque constant K_T , Fig. 7 is a scaled version of Fig. 5. The torque drives the yaw response of the quadrotor without cant. The motor torque response in transfer function form is:

$$\frac{Q_T}{V} = \frac{K(s + \omega_{lead})}{(s + \omega_{mot})(s + \omega_{elec})} \quad (5)$$

Here, the gain K represents the overall gain in the torque response, the zero dynamics are

$$s + \omega_{lead} = s + \frac{B + \partial Q_A / \partial \Omega}{I}$$

and the quadratic roots are

$$(s + \omega_{mot})(s + \omega_{elec}) = \left(s + \frac{R_a}{L_a}\right) \left(s + \frac{B + \partial Q_A / \partial \Omega}{I}\right) + \frac{K_e K_T}{L_a I}$$

The differences in magnitude between Figs. 5 and 7 are a result of the different values of K_T from the two identification processes used. The two poles in the responses are associated with the mechanical motor system overcoming inertia and drag, and the electrical system overcoming inductance and back-EMF, as given in Equation (3).

The thrust response in Fig. 8 is similarly a scaled version of the motor speed response in Fig. 6, since motor thrust is dependent only on rotor speed to generate higher dynamic pressure and lift along the blades. The thrust response has the same poles as the torque response but doesn't contain the zero:

$$\frac{T}{V} = \frac{K}{(s + \omega_{mot})(s + \omega_{elec})} \quad (6)$$

Here K represents a gain that is a function of identified motor constants. The *test stand* K_e results give a $\omega_{mot} = 11.1$ rad/sec and a $\omega_{elec} = 72.5$ rad/sec. The *no load* K_e results give a $\omega_{mot} = 18.4$ rad/sec and a $\omega_{elec} = 32.9$ rad/sec. In both cases, the pole associated with the electrical inductance is at a higher frequency than was tested using the sweep and therefore was omitted from the subsequent identification of the aircraft dynamics. Both models predict a torque response zero at $\omega_{lead} = 5.0$ rad/sec. The subsequent identification results only retain the lead term and a single pole associated with the motor mechanical system response. Even though the *no load* K_e model has a higher mismatch cost, it was used in the final set of comparison results of the different aircraft since the K_e value matched closely to the specified value of the motor.

3.2 Hovering baseline quadrotor

To properly quantify the impacts of the wings and rotor cant, a baseline quadcopter identification was first undertaken. Figures 9–12 show the dynamics of the primary on-axis response for the longitudinal, lateral, heave and yaw axes, respectively. A state-space model was fit to the flight test-based frequency responses, and the resulting model is also shown. The models all represent the bare-airframe dynamics and are obtained from closed-loop data. This can be achieved when turbulence and other disturbances to the feedback loop are minimised, so care was taken to perform flight tests only on calm days.

The dominant dynamics of the baseline quadrotor agree qualitatively with trends observed in prior work [11, 12]. Both motor models were used to demonstrate the similarity between the responses. The *no load* K_e responses have better fits at high frequency, particularly in the phase responses. This is due to the higher motor frequency.

The flight tests were broken into two records to facilitate data collection and piloting; each individual sweep was over two minutes in length, and multiple iterations were performed for each sweep. The lower frequency sweep flight tests ranged from 0.3 to 3 rad/sec, and the higher frequency sweeps ranged from 1.2 rad/sec to 30 rad/sec. The frequency responses generally show high coherence, above $\gamma^2 > 0.6$, indicating quality test data. Drops in coherence are only present in the lateral (Fig. 9) and longitudinal axes (Fig. 10) around $\omega = 3$ rad/sec, where the unstable phugoid dynamics are in both axes. This trend has been observed in past tests [11, 12] as well.

The parameters of the state-space models were generally well identified. The average model mismatch costs in the roll and pitch responses were between $J_{ave} = 50$ and $J_{ave} = 100$, indicating that acceptable models were found. In heave and yaw, the mismatch costs were generally below $J_{ave} = 50$, indicating excellent identification results. Individual parameter values were also well identified, with Cramer-Rao bounds below $CR (\%) < 20\%$ and Insensitivities below $I (\%) < 10\%$ as per guidelines [10].

The state-space models used in the identification are given below. The motor frequency was fixed at the identified value of $\omega_{mot} = 18.4$ rad/sec for all responses, based on the *no load* K_e motor identification results, and the motor dynamics are represented by motor state τ .

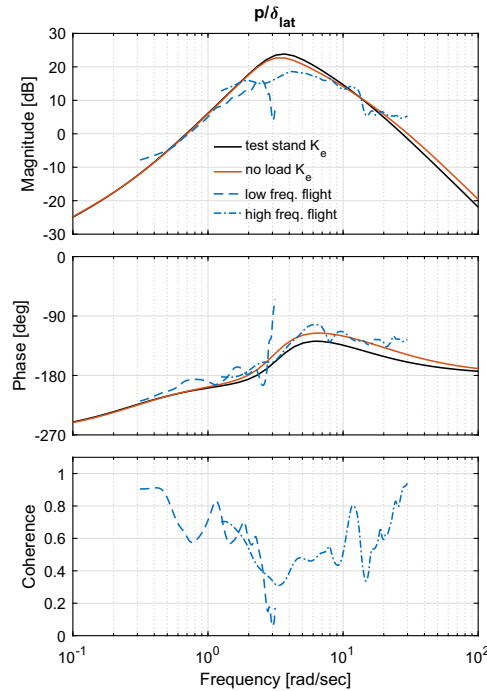


Figure 9. Lateral dynamics response of a hovering quadrotor taken from flight test. Models include motor derivatives using either the identified or no-load K_e values.

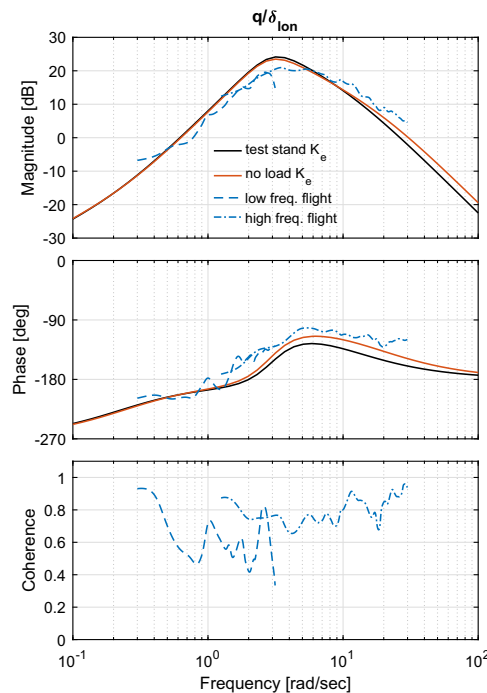


Figure 10. Longitudinal dynamics response of a hovering quadrotor taken from flight test. Models include motor derivatives using either the identified or no-load K_e values.

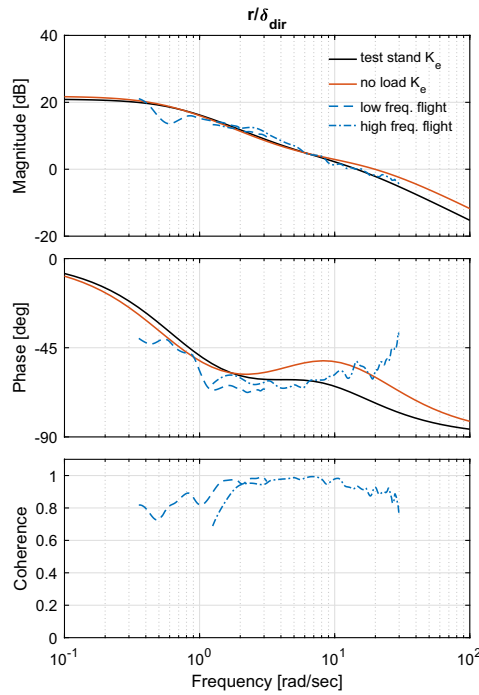


Figure 11. Yaw dynamics response of a hovering quadrotor taken from flight test. Models include motor derivatives using either the identified or no-load K_e values.

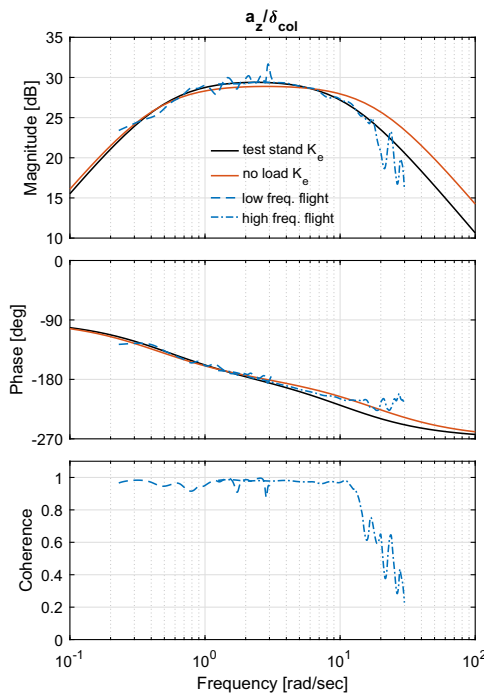


Figure 12. Heave response of a hovering quadrotor taken from flight test. Models include motor derivatives using either the identified or no-load K_e values.

Table 3. Identified longitudinal stability and control derivatives of each configuration

Parameter	Quadrotor	Tailsitter
X_u	-0.2452	-1.895
M_u	2.571	-1.311
M_q	0 ⁺	-1.941
$M_{\delta_{lon}}$	58.97	52.71
ω_{mot}	18.4*	18.4*

*Held constant based on motor subsystem identification.

⁺Fixed at zero to remove parameter insensitivity to model ID result

3.2.1 Pitch and roll dynamics

The pitch axis equations of motion are:

$$\begin{bmatrix} \dot{u} \\ \dot{\theta} \\ \dot{q} \\ \dot{\tau} \end{bmatrix} = \begin{bmatrix} X_u & -g & 0 & 0 \\ 0 & 0 & 1 & 0 \\ M_u & 0 & M_q & M_{\delta_{lon}} \\ 0 & 0 & 0 & -\omega_{mot} \end{bmatrix} \begin{bmatrix} u \\ \theta \\ q \\ \tau \end{bmatrix} + \begin{bmatrix} 0 \\ 0 \\ 0 \\ \omega_{mot} \end{bmatrix} \delta_{lon} \quad (7)$$

For the quadrotor configuration, the pitch damping derivative was not identified, $M_q = 0$, though it is retained since it impacts the pitch dynamics of the tailsitter configuration significantly. Note that the input δ_{lon} drives the motor response, which then drives the pitch moment control derivative $M_{\delta_{lon}}$. This formulation places the control derivative in the matrix of stability derivatives, but allows the model to retain the motor lag dynamics (Equation (6)), which is needed when thrust is used to drive the response in an axis. Figure 10 shows that both models capture the flight test response. The differences in motor modeling appear as a slight phase variation between 3 and 30 rad/sec. Individual parameter values will be compared later with the winged aircraft in Table 3.

The roll axis equations have the same form as the pitch axis equations, with lateral state substituted as appropriate. The roll response in Fig. 9 for the quadcopter configuration is nearly identical to the pitch response due to the symmetry of the vehicle.

3.2.2 Yaw dynamics

The yaw equations of motion are (following the notation from Ivler [12]):

$$\begin{bmatrix} \dot{\psi} \\ \dot{r} \\ \dot{\tau} \end{bmatrix} = \begin{bmatrix} 0 & 1 & 0 \\ 0 & N_r & N_{\delta_{dir}} \\ 0 & 0 & -\omega_{mot} \end{bmatrix} \begin{bmatrix} \psi \\ r \\ \tau \end{bmatrix} + \begin{bmatrix} 0 \\ N'_{\delta_{dir}} \\ \omega_{mot} \end{bmatrix} \delta_{dir} \quad (8)$$

Here a control derivative for yaw is placed in the control derivative matrix, as well as the stability derivative matrix. This formulation gives the motor response a pole/zero dynamics that was shown in Equation (5) and shown in Fig. 7. In transfer function form, the yaw response is:

$$\frac{r}{\delta_{dir}} = \frac{N'_{\delta_{dir}}}{s - N_r} \frac{s + \omega_{lead}}{s + \omega_{mot}} \quad (9)$$

where:

$$\omega_{lead} = \omega_{mot} \left(1 + \frac{N_{\delta_{dir}}}{N'_{\delta_{dir}}} \right) \quad (10)$$

Since the lead frequency was also identified during the motor identification in Equation (5), this equation constrains the two yaw control derivatives $N'_{\delta_{dir}}$ and $N_{\delta_{dir}}$. Solving for $N_{\delta_{dir}}$:

$$N_{\delta_{dir}} = \left(\frac{\omega_{lead}}{\omega_{mot}} - 1 \right) N'_{\delta_{dir}} \quad (11)$$

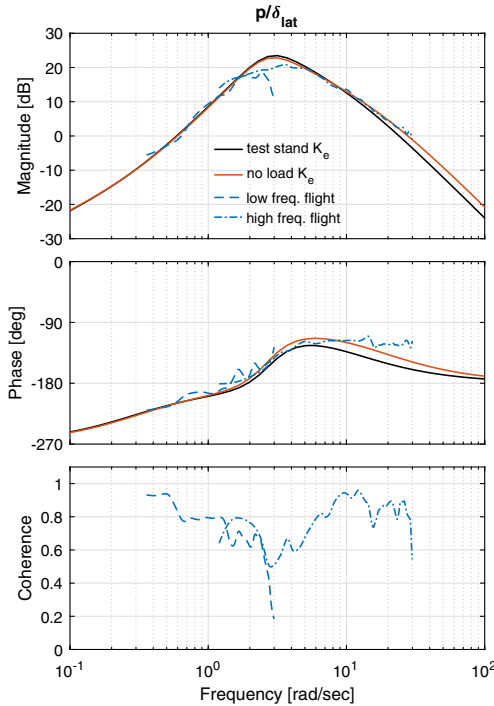


Figure 13. Lateral dynamics response of a hovering tailsitter taken from flight test. Models include motor derivatives using either the identified or no-load K_e values.

For the baseline uncanted quad, which uses pure torque to generate moments, the motor test stand identification resulted in $\omega_{lead}/\omega_{mot} = 5/18.4 = 0.2717$, meaning $N_{\delta_{dir}} = -0.728N'_{\delta_{dir}}$. This leaves only two unknowns in the yaw identification process, N_r , and $N'_{\delta_{dir}}$.

3.2.3 Heave dynamics

Finally, the heave equations are:

$$\begin{bmatrix} \dot{w} \\ \dot{\tau} \end{bmatrix} = \begin{bmatrix} Z_w & Z_{\delta_{col}} \\ 0 & -\omega_{mot} \end{bmatrix} \begin{bmatrix} w \\ \tau \end{bmatrix} + \begin{bmatrix} 0 \\ \omega_{mot} \end{bmatrix} \delta_{col} \quad (12)$$

As with the previous responses, the motor dynamics are held fixed, and only the heave damping Z_w and control derivative $Z_{\delta_{col}}$ are identified.

3.3 Hovering quadrotor biplane tailsitter

Figures 13–16 show the primary on-axis identification results for the baseline tailsitter configuration as pictured in Fig. 1. This configuration was nearly uncontrollable due to poor yaw controllability and an inability of the baseline control system to reject yaw disturbances. However, frequency sweeps were still flown, and a good system identification result was obtained with low model fit mismatch costs.

As with the baseline quad, both motor models are included to highlight the similarity between the responses. The *no load* K_e model shows better alignment in phase for all four axes.

3.3.1 Pitch dynamics

The inclusion of the wing changes the pitch axis system identification in that the pitch damping term M_q needed to be included, whereas the pitch dynamics for the baseline quadrotor were insensitive to

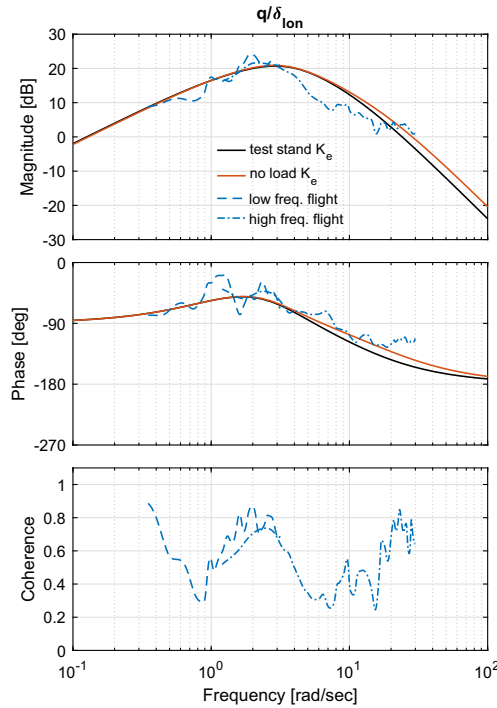


Figure 14. Longitudinal dynamics response of a hovering tailsitter taken from flight test. Models include motor derivatives using either the identified or no-load K_e values.

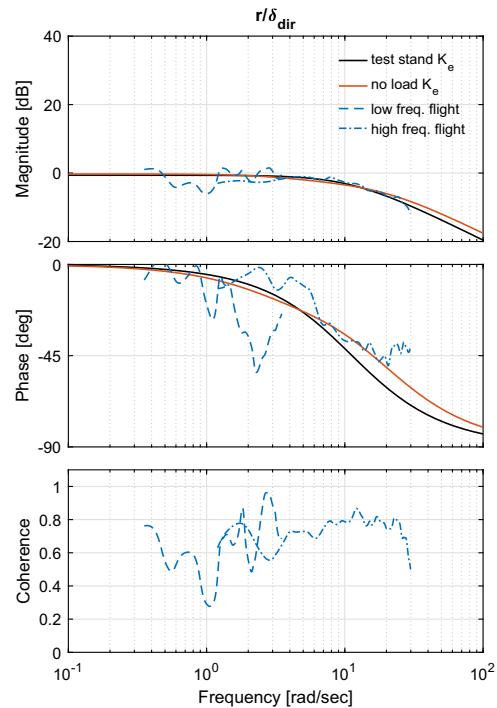


Figure 15. Yaw dynamics response of a hovering tailsitter taken from flight test. Models include motor derivatives using either the identified or no-load K_e values.

Table 4. Comparisons of longitudinal modes for two configurations

Mode	Quadrotor	Tailsitter
Phugoid*	$[-0.48; 2.89]$	$[0.9; 3.19]$
Pitch ⁺	(3.02)	(-1.27)

* $[\zeta; \omega_n]$ is nomenclature for a second order mode, given in terms of damping ratio and natural frequency

⁺(a) is nomenclature for a first order pole $s + a$.

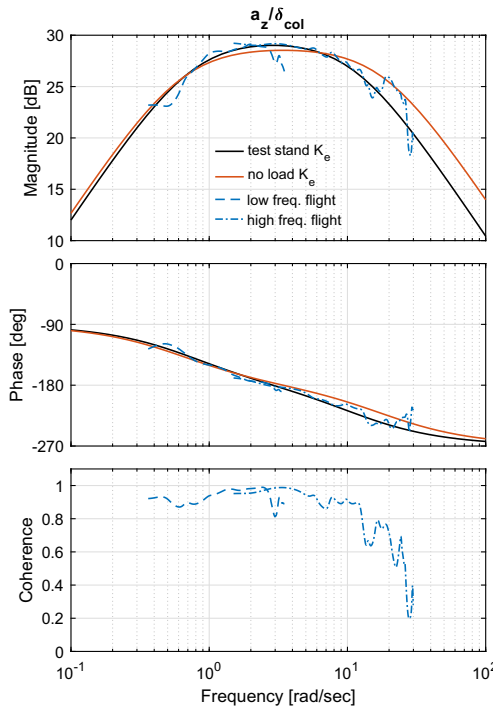


Figure 16. Heave response of a hovering tailsitter taken from flight test. Models include motor derivatives using either the identified or no-load K_e values.

its inclusion. The stability derivatives for the pitch response comparisons are given in Table 3. The tailsitter exhibits nearly a ten-fold increase in drag, derivative X_u , due to the large wings acting like flat plates when forward speed is perturbed. Pitch stability M_u becomes negative, with the wing generating a nose-down moment to forward speed perturbations. As expected, the control derivative $M_{\delta_{lon}}$ remains relatively unchanged. The small decrease may be due to the interactional effects of the wings or the slightly increased pitch inertia resulting from the addition of the foam wings.

The difference in the stability derivatives results in different rigid body modes. The modes are visualised in the Bode plots of Figs. 10 and 14, and their differences are quantified in Table 4. The wing stabilises the Phugoid dynamics, but destabilises the first-order pitch mode.

3.3.2 Yaw dynamics

The yaw axis, Fig. 15, includes the same pole/zero motor dynamics as the response from the baseline quadrotor shown in Fig. 11. The baseline quadrotor yaw damping derivative increased from $N_r = -0.585$ to $N_r = -3.81$ for the tailsitter, a -old increase. This is due to the large wings, which in the hover

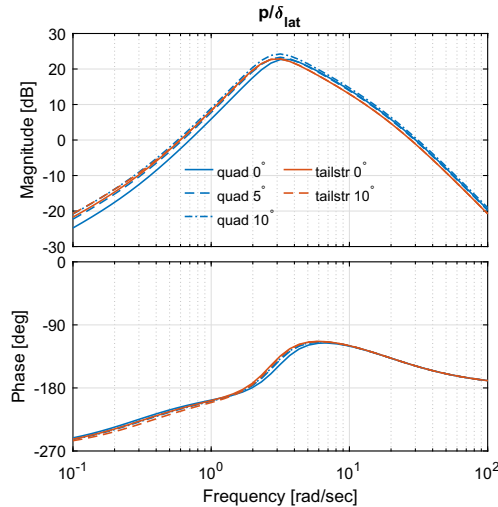


Figure 17. Lateral dynamics response comparisons of identified fit models for the quadrotor and tailsitter configurations with cant angles of 0° , 5° and 10° .

configuration, generate opposing moments when yawed. When evaluated in Equation (9), this increase in yaw damping derivative nearly exactly cancels the zero from the motor dynamics at $\omega_{lead} = 5$ rad/sec, resulting in the first-order appearance of the response at the motor frequency, ω_{mot} .

3.3.3 Roll and heave responses

The roll, Fig. 13, and heave, Fig. 16, responses of the tailsitter configuration remained similar to the baseline quadrotor configuration. The wings produced negligible aerodynamic drag and moments in the hover configuration for these responses. The corresponding roll-damping term L_p was never introduced into the identification. Additional details of the identification of these two responses are omitted for brevity.

3.4 Canted motor results and aircraft comparisons

To investigate the dynamic impact of rotor cant angle, the baseline quadrotor and tailsitter were modified by exchanging the motor mounts with one of two different wedge-shaped mounts. The three blue lines in Figs. 17–20 contain the on-axis response in the four primary control axes. The red lines show the same responses but for the tailsitter. The identified models for motor cants of 0° , 5° and 10° are shown with different line styles. The 5° motor cant was not flown in the tailsitter configuration. The identified model parameters are given in Table 5.

From the figures it is clear that the impact of cant on the on-axis roll, pitch and heave dynamics are negligible, and any observed differences fall within the precision of the model. Further, in the roll and heave responses (shown in Figs. 17 and 20, respectively), all of the configurations are nearly identical, so neither cant nor the wing changes the response significantly in those axes. The differences in the pitch axis can be entirely attributed to the presence of the wing, with no sensitivity to cant angles.

3.4.1 Yaw dynamics

Figure 19 shows that both the wing and cant elicit significant differences in the yaw response for the various configurations, which will be the focus of the discussion herein.

Table 5. Transfer function representations of the yaw response to of each configuration

Parameter	Quadrotor			Tailsitter	
	0°	5°	10°	0°	10°
N_r	−0.5853	−0.7154	−0.7882	−3.806	−3.698
$N_{\delta_{dir}}$	−19.030	−6.969	0.5132	−9.729	−1.657
$N^T_{\delta_{dir}}$	26.23	23.04	24.30	13.41	11.61
ω_{mot}	18.4 ^{&}	18.4 ^{&}	18.4 ^{&}	18.4 ^{&}	18.4 ^{&}
ω_{lead}	5.051	12.835	18.789	5.051	15.774
$\frac{\omega_{lead}}{\omega_{mot}}$	0.275	0.698	1.021	0.275	0.857

[&]Held constant based on motor subsystem identification.

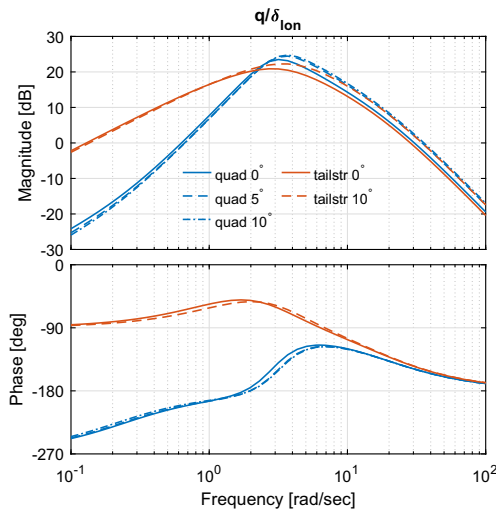


Figure 18. Longitudinal dynamics response comparisons of identified fit models for the quadrotor and tailsitter configurations with cant angles of 0°, 5° and 10°.

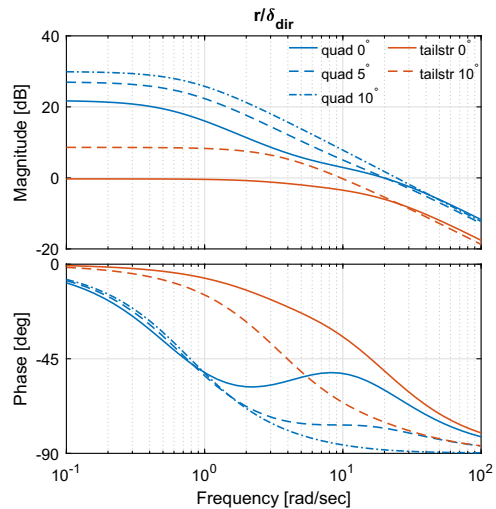


Figure 19. Yaw dynamics response comparisons of identified fit models for the quadrotor and tailsitter configurations with cant angles of 0°, 5° and 10°.

Table 6. Transfer function elements of the yaw response to directional inputs (r/δ_{dir}) of each configuration

Quadrotor			Tailsitter	
0°	5°	10°	0°	10°
26.23 (5.051)	23.04 (12.83)	24.3 (18.79)	13.41 (5.051)	11.61 (15.77)
(0.5853) (18.4)	(0.7154) (18.4)	(0.7882) (18.4)	(3.806) (18.4)	(3.698) (18.4)

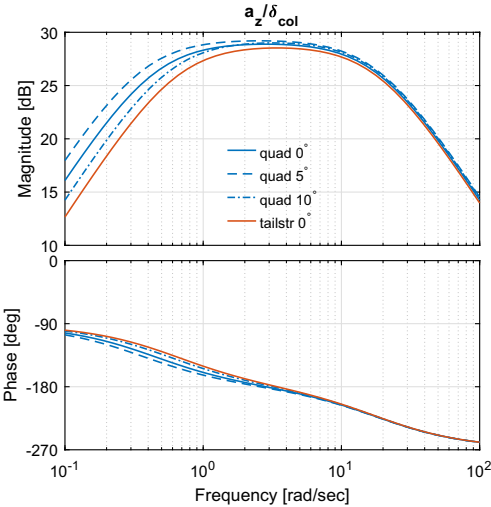


Figure 20. Heave response comparisons of identified fit models for the quadrotor and tailsitter configurations with cant angles of 0°, 5° and 10°.

When compared against the baseline uncanted quadrotor model (which was also shown in Fig. 11), the first-order yaw mode, driven by the yaw damping stability derivative N_r , increases dramatically from around 0.7 rad/sec in the quadrotor to about 4 rad/sec for the tailsitter configuration. This increase in yaw damping is the primary driver of the ten-fold reduction in response magnitude at frequencies below the yaw mode, and degraded the ability for the pilot and baseline control system to control the aircraft and reject disturbances at low frequency. This response magnitude reduction was why the baseline tailsitter was nearly unflyable and frequency sweep flight tests were difficult to perform in all but the calmest days.

The cant angles increase the response magnitude at low frequency. The low frequency yaw response magnitude is doubled (6 dB difference) when 5° of cant is introduced, and increases further when the cant is increased to 10°. The tailsitter was able to be flown satisfactorily with either the 5° or 10° cant angles.

At frequencies above 1 rad/sec, the motor dynamics begin to appear in the 0° cant baseline quadrotor, first with a zero, and then a pole, as shown in Equation (9). These dynamics shift to higher frequencies and have an overall smaller impact on the yaw response as cant angles are introduced. For 5° cant they appear at 2 rad/sec, and are most noticeable in the phase response. For 10° cant angles, the motor response is not noticeable, and the resulting response becomes purely first order. The analytical model in Equation (9) shows that when $\omega_{lead} = \omega_{mot}$, the response from Equation (9) becomes first order since $(s + \omega_{lead}) / (s + \omega_{mot})$ becomes unity when derivative $N_{\delta_{dir}} = 0$. Transfer function representations for the yaw dynamics are shown in Table 6 to better show how the varying zero of the transfer function gives a canceling effect to one of the poles at the different cant angles.

Equation (8) shows the yaw state space model with the stability and control derivatives labeled. The first three columns of Table 5 summarise the corresponding stability and control derivatives for the yaw dynamics of the quadrotor at each cant angle. The reduction of the magnitude of derivative $N_{\delta_{dir}}$, and the resulting trend towards $\omega_{lead}/\omega_{mot} = 1$ is clearly observed.

At the highest frequencies, responses approach the torque control derivative and have a response of $N'_{\delta_{dir}}/s$. The difference in magnitude of $N'_{\delta_{dir}}$ between the tailsitter and quadrotor is primarily driven by the differences in yaw inertia between the two aircraft.

Lastly, a secondary effect of the cant angle is a slight increase in yaw damping (N_r). This could possibly be attributed to an increasing cant angle introducing a component of the free stream velocity to the inflow of the rotors, and more strongly coupling rotor aerodynamic thrust and torque production to yaw rate. This trend is not observed in the tailsitter, which may be due to the much larger impact of the wings on yaw damping or aerodynamic interactions between the rotors and wings.

4.0 Discussion and Conclusions

A quadrotor was modified by adding wings to the frame to directly compare a quadrotor and biplane tailsitter. Canting the motors was also tested to quantify the effects of rotor cant on the dynamics response. The on-axis responses of the aircraft were evaluated through flight test and system identification. Different methods of identifying the full vehicle dynamics demonstrated that identifying the motor torque and back-EMF constants from no-load measurements and the remaining motor parameters from rotor-motor test stand provided the most accurate identified full vehicle model.

For the baseline quadrotor yaw response, differential motor torque is the only control mechanism. The motor torque response is relatively fast and generates both RPM changes and increases in aerodynamic drag. The motor test results show the peak magnitude of the motor response occurring at 25 rad/sec. Canting introduces a moment about the CG from the thrust response. The thrust response for the isolated rotor was shown to be first order, but is slower (occurs at lower frequency) than the torque response since aerodynamic thrust increases through rotor RPM. The results show that relatively small cant angles of 5° are adequate enough for the thrust-based moment to dominate the mid-frequency response between 2 and 10 rad/sec, where the torque is degraded from its peak. Above 10 rad/sec, the torque-based response acts quickly to generate yaw moments as the rotor RPM is increased. In this sense, canting allows the yaw axis to benefit from both the thrust and torque responses to generate yaw moments.

Based on the data and analysis presented, the following conclusions can be drawn:

- A motor model is required to correctly capture the dynamics of quadrotor vehicles. The higher frequency electrical system dynamics have a smaller impact and can be omitted for flight dynamics purposes.
- The yaw axis saw an increase in the yaw damping derivative, due to the wing being attached, and a reduction in the yaw control derivative, primarily due to the increased inertia. The biplane tailsitter with no cant was extremely difficult to control adequately in the yaw axis.
- By introducing cant, both the quadrotor and tailsitter saw increases in the aircraft yaw response magnitude. Further, the rotor thrust-based moment generation due to cant resulted in the yaw response zero being canceled by the motor dynamics, resulting in a purely first-order yaw response with the yaw mode being at the motor model frequency.
- Neither the wing nor cant produced any significant changes in the lateral and heave axes.

Acknowledgements. The authors would like to thank Mr. Steve Galindo for his technical expertise and support in the manufacture, assembly and flight testing of the various vehicles used in this paper. Mr. Galindo's help was invaluable in collecting nearly all the data used in this paper.

This is a work of the U.S. Government and is not subject to copyright protection in the United States.

References

- [1] Hrishikeshavan, V., Bawek, D., Rand, O. and Chopra, I. Control of a quad rotor-biplane micro air vehicle in transition from hover to forward flight, *American Helicopter Society Specialists' Meeting for Unmanned Rotorcraft Proceedings*, Scottsdale, AZ, Jan 2013.
- [2] Hrishikeshavan, V., Yeo, D. and Chopra, I. Onboard flow sensing in a quadrotor biplane micro air vehicle for transition between hover and steady-level flight, *American Helicopter Society Specialists' Meeting for Unmanned Rotorcraft Proceedings*, Chandler, AZ, Jan 2015.
- [3] Singh, R., Hrishikeshavan, V. and Sirohi, J. Common research configuration for collaborative advancement of scalable VTOL UAS technologies, *Vertical Flight Society 75th Annual Forum Proceedings*, Philadelphia, PA, May 2019.
- [4] Reddinger, J.P. Performance and control of a scalable quadrotor biplane tailsitter, *AIAA Scitech 2019 Forum Proceedings*, San Diego, CA, Jan 2019.
- [5] Misiorowski, M., Gandhi, F. and Anusonti-Inthra, P. Computational analysis of rotor-Blown-Wing for eVTOL applications, *Vertical Flight Society 75th Annual Forum Proceedings*, Philadelphia, PA, May 2019.
- [6] Gupta, S., Abhishek, A., and Kothari, M., Physics based flight dynamic modeling for biplane tailsitter during forward transition, *Vertical Flight Society 79th Annual Forum Proceedings*, West Palm Beach, FL, May 2023.
- [7] Phillips, B., Hrishikeshavan, V., Rand, O. and Chopra, I. Onboard flow sensing in a quadrotor biplane micro air vehicle for transition between hover and steady-level flight, *American Helicopter Society 72nd Annual Forum Proceedings*, West Palm Beach, FL, May 2016.
- [8] Atci, K., Jusko, T., Strbak, A. and Guner, F. Impact of differential torsional rotor cant on the flight characteristics of a passenger-grade quadrotor, *CEAS Aeronaut J*, Jan 2024. DOI: [10.1007/s13272-023-00705-7](https://doi.org/10.1007/s13272-023-00705-7)
- [9] Torno, H., Armstrong, B., Munsell, G., Galindo, S. and Juhasz, O. System identification and flight dynamics analysis of a quad-biplane tail-sitter aircraft in hover, *AIAA SciTech 2023 Forum Proceedings*, National Harbor, MD, Jan 2023.
- [10] Tischler, M.B. and Remple, R.K. Aircraft and rotorcraft system identification: engineering methods with flight test examples, AIAA, 2nd ed. Reston, VA, 2012. DOI: [10.2514/4.868207](https://doi.org/10.2514/4.868207)
- [11] Cheung, K.K., et al., An overview of the US army aviation development directorate quadrotor guidance, navigation, and control project, *AHS International 73rd Annual Forum Proceedings*, Fort Worth, TX, May 2017.
- [12] Ivler, C.M., Rowe, E.S., Martin, J., Lopez, M.J.S. and Tischler, M.B., System identification guidance for multirotor aircraft: dynamic scaling and test techniques, *Vertical Flight Society 75th Annual Forum Proceedings*, Philadelphia, PA, May 2019.
- [13] Gong, A., Sanders, F.C., Hess, R.A. and Tischler, M.B. System identification and full flight-envelope model stitching of a package-delivery octocopter, *AIAA Scitech 2019 Forum*, 2019. DOI: [10.2514/6.2019-1076](https://doi.org/10.2514/6.2019-1076)
- [14] Malpica, C. and Withrow-Maser, S. Handling qualities analysis of blade pitch and rotor speed controlled eVTOL quadrotor concepts for urban air mobility, *VFS International Powered Lift Conference Proceedings*, San Jose, CA, 2020.